PCCP

ROYAL SOCIETY OF CHEMISTRY

PAPER

View Article Online
View Journal | View Issue

Cite this: *Phys. Chem. Chem. Phys.*, 2025, **27**, 10185

Spectral mechanisms of solid/liquid interfacial heat transfer in the presence of a meniscus†

Abdullah El-Rifai, *[a] Liudmyla Klochko, [b] Viktor Mandrolko, [c] Sreehari Perumanath,[d] David Lacroix, [c] Rohit Pillai*[a] and Mykola Isaiev *[c]

In this study, we employ molecular simulations to investigate the enhancement in thermal conductance at the solid/liquid interface in the presence of a meniscus reported previously (Klochko *et al.*, *Phys. Chem. Chem. Phys.*, 2023, **25**(4), 3298–3308). We vary the solid/liquid interaction strength at Lennard-Jones interfaces for both confined liquid and meniscus systems, finding that the presence of a meniscus yields an enhancement in the solid/liquid interfacial thermal conductance across all wettabilities. However, the magnitude of the enhancement is found to depend on the surface wettability, initially rising monotonously for low to moderate wettabilities, followed by a sharp rise between moderate and high wettabilities. The spectral decomposition of heat flux formalism was applied to understand the nature of this phenomenon further. By computing the in-plane and out-of-plane components of the heat fluxes within both the interfacial solid and liquid, we show that the initial monotonous rise in conductance enhancement predominantly stems from a rise in the coupling of out-of-plane vibrations within both the solid and the liquid. In contrast, the subsequent sharp rise at more wetting interfaces is linked to sharp increases in the utilization of the in-plane modes of the solid and liquid. These observations result from the interplay between the solid/liquid adhesive forces and the liquid/vapor interfacial tension. Our results can aid engineers in optimizing thermal transport at realistic interfaces, which is critical to designing effective cooling solutions for electronics, among other applications.

Received 18th December 2024,
Accepted 11th April 2025

DOI: 10.1039/d4cp04768k

rsc.li/pccp

Introduction

The thermal transport across the region where the solid, liquid, and gas phases intersect, known as the "three-phase contact line" (TPCL), is key to phase-change processes,[1,2] and impacts the performance of state-of-the-art two-phase cooling solutions for integrated circuits.[3] Recently, for example, candidate cooling devices have been developed where high heat flux dissipation is achieved by inducing evaporation from menisci pinned within nanoporous membranes.[4,5] Given the importance of the heat transfer at the TPCL in such devices, as well as its relevance to other practical applications such as scanning thermal microscopy,[6–8] phase change materials,[9,10] and photo-thermally induced bubble growth,[11] gaining a better understanding of the energy transport at such interfaces is becoming increasingly important.

Despite the nanoscale dimensions of the TPCL (shown to reach <30 nm experimentally[12]), several experimental and numerical studies have demonstrated that it plays a major role in evaporative heat transfer. Stephan and Busse[13] found that half of the heat transferred within a grooved heat pipe evaporator occurred across the TPCLs of the liquid menisci. Ibrahem *et al.*[14] studied the heat transfer characteristics at the TPCL of a liquid meniscus pinned in a microchannel, finding that the peak evaporative heat flux occurs at the TPCL. Kunkelmann *et al.*[15] reported similar findings for advancing and receding menisci. Maroo and Chung[16] simulated evaporation from nanoscale menisci, similarly reporting that the maximum evaporative heat flux occurs from the TPCL. Thus, to improve the rate of heat transfer in such systems, the energy transport at the TPCL must be better understood.

Numerous studies have reported that the overall heat transfer from evaporating TPCLs is impacted by the interfacial thermal conductance across the solid/liquid interface (Γ), which manifests as a temperature discontinuity at the interface (ΔT), and is related to the solid/liquid area of contact (A_c) and the heat transferred across this area (Q) *via* $\Gamma = Q/A_c\Delta T$. Zhao *et al.*[17] investigated evaporation processes in microchannels using kinetic theory, finding that Γ can reduce the peak evaporative heat flux from the TPCL by approximately 15%. Han *et al.*[18] and Ma *et al.*[19] studied thin-film evaporation using molecular dynamics

[a] *Institute for Multiscale Thermofluids, University of Edinburgh, Edinburgh EH9 3FD, UK. E-mail: abdullah.elrifai@hotmail.com, r.pillai@ed.ac.uk*
[b] *Université de Lorraine, LORIA, Nancy F-54000, France*
[c] *Université de Lorraine, CNRS, LEMTA, Nancy F-54000, France. E-mail: mykola.isaiev@univ-lorraine.fr*
[d] *Department of Mechanical Engineering, Indian Institute of Technology Madras, Chennai 600036, India*

† Electronic supplementary information (ESI) available. See DOI: https://doi.org/10.1039/d4cp04768k

(MD) simulations, finding that Γ can bottleneck evaporative heat transfer by up to 20% for regions of the TPCL where the liquid films become ultra-thin (<100 nm thick). Thus, a deeper understanding of Γ in the presence of the TPCL can help enhance the rate of evaporative heat transfer in such processes.

Klochko *et al.*[20] investigated interfacial energy transport at the TPCL of a silicon/water interface for various surface wettabilities using a combination of MD and finite element method simulations. To understand how the presence of the TPCL influenced energy transport, they studied two distinct systems: (i) a system in which the silicon walls fully confined the water and thus had an absence of vapor, referred to as the "confined" system, and (ii) a system that contained TPCLs induced by pinning a water meniscus between two silicon walls, denoted as the "meniscus" system. In the confined system, the interfacial energy transport was determined by the total interfacial thermal conductance ($G = Q/A\Delta T$), where A is the cross-sectional area of the solid. In the meniscus system, there were comparatively fewer liquid atoms, which made a reduced area of contact with the solid (A_c) and led to a reduction in the total thermal conductance G of the interface. However, when computing the solid/liquid thermal conductance of the two systems Γ, Klochko *et al.*[20] found that the presence of a meniscus led to a localized "enhancement" in Γ across all surface wettabilities, which is to say that greater heat is transported than expected once the reduction in contact area is accounted for. Note that this does not imply that the interface at a meniscus system transfers more thermal energy in total than the confined system. However, this localized enhancement is still unexpected and therefore noteworthy, and its origins have not yet been understood.

While studies on the enhancement of Γ at the TPCL are sparse, efforts have been made to uncover the origins of enhancements in Γ at solid/liquid interfaces through the analysis of the structural properties of the interfacial liquid. Shenogina *et al.*[21] observed that Γ exhibits a linear relationship with the work of adhesion at self-assembled-monolayer/water interfaces; however, other studies have reported that this cannot be used as the sole predictor of Γ.[22–24] Alexeev *et al.*[25] reported a correlation between the peak interfacial density of the liquid and Γ at a graphene/water interface, but other studies have shown that this correlation does not always hold.[24,26–31] Ramos-Alvarado *et al.*[32] demonstrated a correlation between the density depletion length and Γ at a silicon/water interface, however this could not be successfully applied to other interfaces.[28,31,33–35] Ma *et al.*[26] demonstrated that the increase in Γ due to the presence of surface charges at a graphene/water interface was linked to a rise in the in-plane ordering of the interfacial liquid, but other studies have shown that this is not universally applicable.[27,28,36] While structural properties have been partially successful in explaining increases in Γ, their lack of universality means other approaches must be sought to fully understand the origins of enhancements in Γ.

An alternative method to gain insights into enhancements in Γ revolves around deploying *spectral* techniques to directly probe the behavior of the interfacial atomic vibrations, the sole energy carriers across electrically non-conductive interfaces.[37] In a number of studies, the enhancements in Γ were attributed to a change in the *frequencies* of the vibrations engaged in interfacial heat transfer, referred to as "utilized" modes. Qian *et al.*[38] found that the rise in Γ with increasing surface wettability at a graphene/ionic–liquid interface was linked to a rise in the utilization of high-frequency modes within the interfacial solid. Ma *et al.*[26] demonstrated that the enhancement in Γ yielded by an increase in the magnitude of surface charges at a graphene/water interface is similarly associated with greater high-frequency mode utilization in the interfacial solid. Qian *et al.*[39] reported a comparable effect at graphene/ionic–liquid interfaces with increasing surface charge magnitude. In our previous work,[40] we demonstrated that the exponential-to-linear regime cross-over that Γ experiences with increasing solid/liquid interaction strength (ε_{SL}) at LJ interfaces is related to an increase in the similarity of the frequencies of the utilized vibrations within the interfacial solid and liquid. The successful implementation of spectral techniques to understand enhancements in Γ at solid/liquid interfaces in these studies raises the following question for the TPCL system of interest here: *does the presence of a TPCL similarly alter the frequencies of the vibrations utilized, and does that spectral variation enhance Γ?*

In other studies, the increases in Γ at solid/liquid interfaces were also found to be linked to the *orientation* of the utilized vibrations with respect to the plane of the interface. Note that vibrational modes can be classified by orientation into: (i) in-plane (*i.e.* parallel to the interface), and (ii) out-of-plane (*i.e.* perpendicular to the interface) vibrations. Ramos-Alvarado and Kumar[33] found that the rise in Γ with increasing wettability at silicon/water interfaces was linked to greater high-frequency mode utilization, as well as increased in-plane mode utilization in the solid. Gonzalez-Valle and Ramos-Alvarado[35] reported similar findings at a silicon–carbide/water interface. Zhou *et al.*[41] demonstrated that the rise in Γ induced by the presence of atomic defects at a graphene/hydrocarbon interface is similarly associated with greater in-plane mode utilization in the solid. These studies raise the second question about the TPCL-induced enhancement in Γ: *does the presence of a TPCL influence the orientation of the vibrations utilized, and does that spectral variation enhance Γ?*

Klochko *et al.*[20] hypothesized that the enhancement in Γ in the presence of the TPCL stems from greater in-plane mode utilization in the interfacial solid; however, this hypothesis was not quantified using spectral techniques. In our previous work,[40] the exponential-to-linear regime cross-over in Γ was explained by analyzing both the modes utilized within the solid to transmit energy to the liquid, as well as the modes within the liquid used to *receive* energy from the solid at a Lennard-Jones (LJ) interface. Therefore, in this work, the vibrations utilized within both the solid and liquid will be analyzed for the first time to understand the origin of the enhancement in Γ yielded by the presence of a TPCL at a simple LJ interface.

Methodology

System setup

We conduct non-equilibrium MD simulations using LAMMPS[42] to investigate the origin of the enhancement in interfacial

energy transport at an LJ interface. We consider two systems: (i) a liquid fully confined between the walls of a nanochannel, referred to as the "confined" system (Fig. 1(a)), and (ii) a partially filled nanochannel comprising a meniscus, referred to as the "meniscus" system (Fig. 1(b)). The meniscus system was generated by removing the top and bottom 1/3rd of liquid atoms in the y-direction from the confined system. The confined system comprises 5157 liquid atoms, while the meniscus system comprises 1719 liquid atoms. The system geometry is identical for both the confined and meniscus systems. The nanochannel width is set to $L_{\text{liquid}} \approx 30$ Å. The cross-sectional area of the domain A_{wall} is set to $18 \times 18\ a^2$, where $a = 5.304$ Å is the lattice constant of the FCC solid. The [100] crystallographic planes of the walls are oriented along the direction of the heat flux. The wall thickness is set to $L_{\text{wall}} = 12a$. In both systems, each wall is composed of 15 552 solid atoms. The domain is periodic in all dimensions except the x-direction, for which a 'fixed' boundary condition is used.

Systems are initially relaxed using an energy minimization step. Following this, simulations are initiated with an equilibration stage at 70 K under the NVT ensemble for 5 ns for both systems, with a timestep of 1 fs. In the case of the confined system, the pressure is controlled by applying a piston to the right wall to achieve the pressure corresponding to 1 atm. After the equilibration stage, the piston condition is removed, and the outermost green-colored solid layers at both ends of the simulation domain (see Fig. 1) are held rigid to maintain the specified pressure as well as avoid the displacement of the interfaces. The red-colored solid atoms in the left wall (tagged as L_{heat} in Fig. 1) are then set to $T_{\text{hot}} = 80$ K, while the blue-colored atoms in the right wall (tagged as L_{cool} in Fig. 1) are set to $T_{\text{cold}} = 60$ K, using a Nosé–Hoover thermostat under the NVT ensemble. The solid atoms in the gray portions of both walls, all liquid atoms, and any vapor atoms are permitted to vibrate freely using the NVE ensemble. The system is thermalized under these conditions for 3 ns to ensure a steady state is reached. Afterwards, a data production run is conducted by running the simulation for an additional 10 ns, sampled every 1000 time steps.

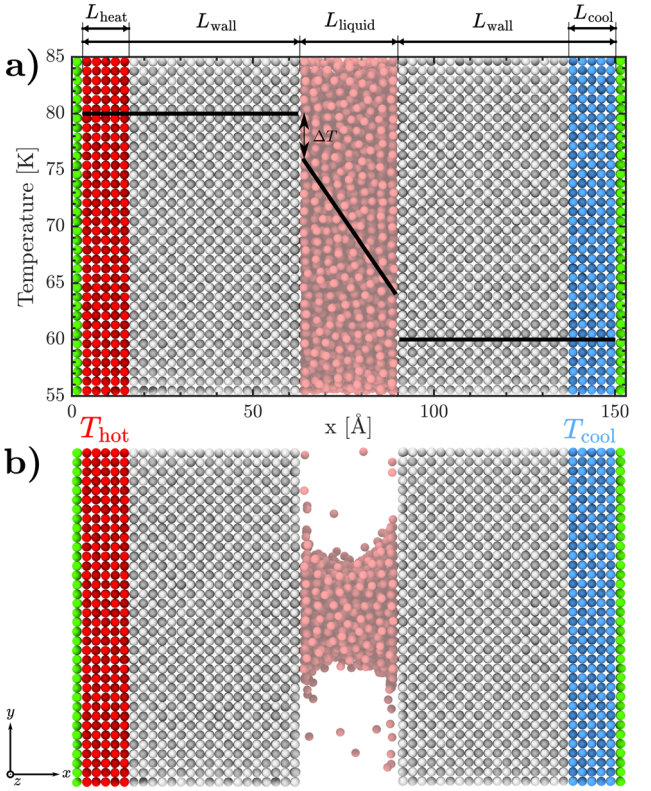

Fig. 1 (a) A nanochannel comprising two LJ FCC [100] walls of length L_{wall} separated by a distance L_{liquid}, completely filled with a Lennard-Jones (LJ) liquid. The red-colored solid atoms in the left wall represent the atoms to be thermostatted to $T_{\text{hot}} = 80$ K during the thermalization of the system, while the blue-colored atoms in the right wall represent the atoms to be thermostatted to $T_{\text{cold}} = 60$ K during the thermalization phase. The green-colored layer of solid atoms in both walls are held rigid, while the gray-colored solid atoms are allowed to vibrate freely. The temperature gradient within all materials is shown using solid black lines, with the solid/liquid interfacial discontinuity ΔT highlighted using black arrows. (b) The same nanochannel is only partially filled with an LJ meniscus.

All interatomic interactions are modeled using the LJ potential[43] using a cut-off distance $r_{\text{cut}} = 8.5$ Å. In line with prior studies on LJ interfaces,[40,44,45] the liquid/liquid interaction strength is set to $\varepsilon_{\text{LL}} = 10.3$ meV, while the solid/solid interaction strength is set to $\varepsilon_{\text{SS}} = 10\varepsilon_{\text{LL}}$. For all interactions, the length scale in the LJ potential is kept at $\sigma = 3.405$ Å. All atomic masses m are set to 40.0 amu. To quantify the impact of the surface wettability on solid/liquid interfacial energy transport, the solid/liquid interaction strength ε_{SL} is varied directly in the range from 2.5 meV to 7.5 meV. The resulting wetting angles (θ) corresponding to all values of ε_{SL} were calculated from the density profiles similar to Isaiev *et al.*,[46] and are presented in Fig. 2. MD snapshots of the resulting meniscus shape are illustrated in the insets. The range of values for ε_{SL} is chosen such that menisci of various curvatures are produced, with the transition from phobicity to philicity occurring around $\varepsilon_{\text{SL}} \approx 5$ meV, as observed in Fig. 2. The maximum value of ε_{SL} is chosen so the meniscus does not thoroughly wet the surface. The interaction energies, temperatures, and system geometry are provided in LJ reduced units in Table S1 of the ESI.†

Calculation of the interfacial thermal conductance

The presence of thermostats at both ends of the domain which are 20 K apart produces a linearly varying temperature distribution within the domain (shown using black lines in Fig. 1(a)). The consequent interfacial temperature discontinuity at the solid/liquid interface (ΔT) can be calculated by extrapolating the best-fit line through the bulk liquid's temperature field to the interfacial solid in the left wall. The solid/liquid interfacial thermal conductance (Γ) is then computed using

$$\Gamma = \frac{Q}{\Delta T A_{\text{c}}}, \tag{1}$$

where Q is the heat transferred across the interface, and A_{c} is the actual solid/liquid contact area. To determine A_{c} in each case, the density profile of the liquid is computed (see Fig. S1, ESI†). Following this, the intersection coordinates between the liquid and substrate along the in-plane direction are identified. The contact area is then determined by multiplying the intersection points along the y and z axes. Note that in the confined case, A_{c} is equivalent to

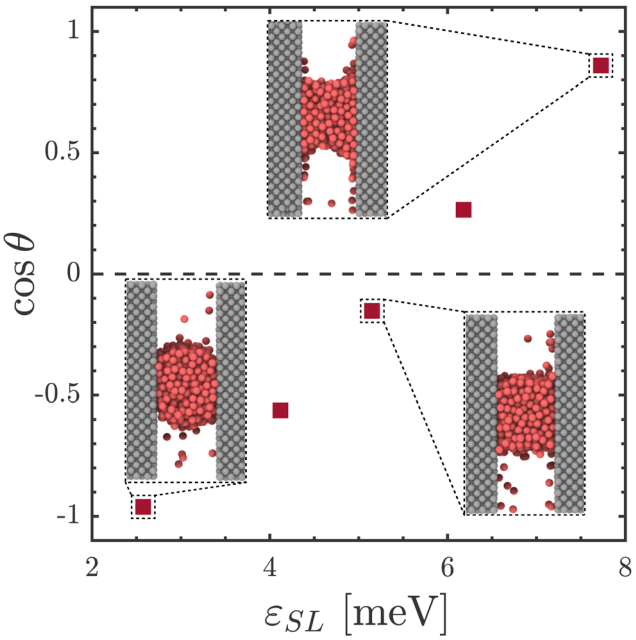

Fig. 2 The relationship between the cosine of the contact angle that the liquid makes with the surface (θ) and ε_{SL}. The insets depict the shape of the meniscus at various values of ε_{SL}.

the cross-sectional area of the wall A_{wall}, *i.e.* $A_c = A_{wall}$, while in the meniscus case $A_c < A_{wall}$.

Spectral analysis of the interfacial thermal conductance

The spectral analysis of interfacial heat transfer can be conducted using the methodology developed by Sääskilahti *et al.*,[44] and validated for liquids of varying wettability in our previous work.[40] Through this, the spectral decomposition of heat flux within the interfacial solid $q(\omega)_{L\to S}$ can be computed, which quantifies the contributions of each vibration of frequency ω utilized within the solid to *transmit* energy to the liquid. It can be derived from the Fourier transform of the cross-correlation between the cumulative forces that all liquid atoms exert upon each solid atom and the velocities of the solid atoms *via*:

$$q(\omega)_{L\to S} = \frac{2}{A_c}\cdot\Re\left(\sum_{i\in L}\sum_{j\in S}\int_{-\infty}^{\infty} d\tau\, e^{i\omega\tau}\left\langle \vec{F}^{ij}_{L\to S}(\tau)\cdot\vec{v}_j(0)\right\rangle\right), \quad (2)$$

where τ is the correlation time between forces and velocities; $\vec{F}^{ji}_{L\to S}$ is the force acting on the j-th atom of the solid from the i-th atom of the liquid; and $\vec{v}_i$ and $\vec{v}_j$ are the velocities of the i-th and j-th atom respectively, as illustrated in Fig. 3.

The spectral decomposition of heat flux within the interfacial liquid $q(\omega)_{S\to L}$, which instead quantifies the contributions of each vibration of frequency ω utilized within the liquid to *receive* energy from the solid, can be calculated using a similar approach. It can be derived from the Fourier transform of the cross-correlation between the cumulative forces that all solid atoms exert upon each liquid atom and the velocities of the liquid atoms *via*:

$$q(\omega)_{S\to L} = \frac{2}{A_c}\cdot\Re\left(\sum_{i\in L}\sum_{j\in S}\int_{-\infty}^{\infty} d\tau\, e^{i\omega\tau}\left\langle \vec{F}^{ji}_{L\to S}(\tau)\cdot\vec{v}_i(0)\right\rangle\right), \quad (3)$$

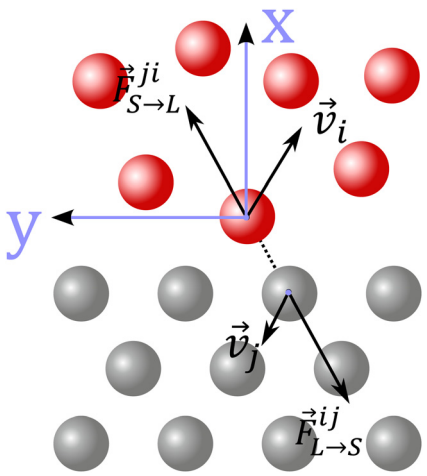

Fig. 3 Schematic representation of the interactions between atoms of a solid and a liquid.

where τ is the correlation time between forces and velocities; $\vec{F}^{ji}_{S\to L}$ is the force acting on the i-th atom of the liquid from the j-th atom of the solid; and $\vec{v}_i$ and $\vec{v}_j$ are the velocities of the i-th and j-th atom respectively, similarly depicted in Fig. 3.

In order to consider the *orientation* of the vibrations, rather than merely their *frequency*, the directional components of the force and velocity vectors must be considered independently. The utilization of out-of-plane vibrations ($q^{\perp}_{L\to S}$ and $q^{\perp}_{S\to L}$) is computed using the component of the forces and velocities vectors that is perpendicular to the interface, *via*:

$$q(\omega)^{\perp}_{L\to S} = \frac{2}{A_c}\cdot\Re\left(\sum_{i\in L}\sum_{j\in S}\int_{-\infty}^{\infty} d\tau\, e^{i\omega\tau}\left\langle \left(\vec{F}^{ij}_{L\to S}(\tau)\right)_x\cdot\left(\vec{v}_j(0)\right)_x\right\rangle\right), \quad (4)$$

and

$$q(\omega)^{\perp}_{S\to L} = \frac{2}{A_c}\cdot\Re\left(\sum_{i\in L}\sum_{j\in S}\int_{-\infty}^{\infty} d\tau\, e^{i\omega\tau}\left\langle \left(\vec{F}^{ji}_{S\to L}(\tau)\right)_x\cdot\left(\vec{v}_i(0)\right)_x\right\rangle\right). \quad (5)$$

Similarly, the utilization of in-plane modes ($q^{\parallel}_{L\to S}$ and $q^{\parallel}_{S\to L}$) is obtained from the components of the force and velocity vectors that are parallel to the interface, as follows:

$$q(\omega)^{\parallel}_{L\to S} = \frac{2}{A_c}\cdot\Re\left(\sum_{i\in L}\sum_{j\in S}\int_{-\infty}^{\infty} d\tau\, e^{i\omega\tau}\left(\left\langle \left(\vec{F}^{ij}_{L\to S}(\tau)\right)_y\cdot\left(\vec{v}_j(0)\right)_y\right\rangle + \left\langle \left(\vec{F}^{ij}_{L\to S}(\tau)\right)_z\cdot\left(\vec{v}_j(0)\right)_z\right\rangle\right)\right), \quad (6)$$

and

$$q(\omega)^{\parallel}_{\mathrm{S}\to\mathrm{L}} = \frac{2}{A_c}\cdot\Re\left(\sum_{i\in L}\sum_{j\in S}\int_{-\infty}^{\infty} \mathrm{d}\tau\, e^{i\omega\tau}\left(\left\langle\left(\vec{F}^{ij}_{\mathrm{S}\to\mathrm{L}}(\tau)\right)_y\cdot(\vec{v}_i(0))_y\right\rangle + \left\langle\left(\vec{F}^{ij}_{\mathrm{S}\to\mathrm{L}}(\tau)\right)_z\cdot(\vec{v}_i(0))_z\right\rangle\right)\right). \quad (7)$$

From the separate components of the $q(\omega)$, the cumulative thermal conductance across the solid/liquid interface can be calculated for both in-plane and out-of-plane modes as follows:

$$\Gamma(\omega)^{\perp,\parallel}_{\mathrm{L}\to\mathrm{S,S}\to\mathrm{L}} = \frac{1}{\Delta T}\int_0^{\omega} q(\omega)^{\perp,\parallel}_{\mathrm{L}\to\mathrm{S,S}\to\mathrm{L}}\frac{\mathrm{d}\omega}{2\pi}, \quad (8)$$

and the total one:

$$\Gamma(\omega)_{\mathrm{L}\to\mathrm{S,S}\to\mathrm{L}} = \Gamma(\omega)^{\perp}_{\mathrm{L}\to\mathrm{S,S}\to\mathrm{L}} + \Gamma(\omega)^{\parallel}_{\mathrm{L}\to\mathrm{S,S}\to\mathrm{L}}. \quad (9)$$

In the computation of eqn (2)–(9), all solid and liquid atoms within the interaction cut-off distance r_{cut} are considered.

Results & discussion

Effect of meniscus on Γ at various values of ε_{SL}

In Fig. 4(a), the variation of Γ with ε_{SL} is presented for the meniscus and confined systems as obtained through eqn (1). With rising ε_{SL}, Γ increases steadily for both systems. However, it can be observed that the magnitude of Γ in the meniscus system is larger than that of the confined system. This implies that the presence of a meniscus yields an enhancement in Γ across all values of ε_{SL}. This enhancement is denoted as $\Delta\Gamma = \Gamma_{\mathrm{meniscus}} - \Gamma_{\mathrm{confined}}$, and is illustrated for the $\varepsilon_{SL} \approx 6$ meV case in Fig. 4(a). To rule out the possibility that the observed enhancement in Γ is caused by system size effects, we conducted two additional simulations for confined and meniscus systems at $\varepsilon_{SL} = 5$ meV where the nanochannel width L_{liquid} was increased to $\approx$80 Å and the interaction cut-off distance r_{cut} was increased to 13 Å. As shown in Table S2 of the ESI,† the presence of a meniscus leads to a notable enhancement in Γ, demonstrating that the reported enhancement in Γ is not related to the nanochannel width.

Klochko *et al.*[20] observed a similar enhancement in Γ caused by the presence of a meniscus at a realistic silicon/water interface. While such realistic interfaces possess complex interfacial forces (*e.g.* electrostatic interactions, hydrogen bonding) that influence interfacial structure,[47–51] which consequently influences heat transfer,[26,38,39] the simplified LJ system investigated in this study is capable of reproducing the enhancement in Γ reported at a realistic silicon/water interface. This makes it an ideal starting point in elucidating the spectral origins of the enhancement in Γ.

Next, $\Delta\Gamma$ is calculated for all values of ε_{SL}, as shown in Fig. 4(b). With increasing ε_{SL}, $\Delta\Gamma$ is seen to increase monotonously until $\varepsilon_{SL} \approx 5$ meV. However, there is a discontinuity at $\varepsilon_{SL} \approx 5$ meV, and it can be observed that $\Delta\Gamma$ experiences a sharp increase beyond this point. This indicates that, while the presence of a meniscus enhances Γ regardless of ε_{SL}, the magnitude of this enhancement is dependent on ε_{SL}. From Fig. 2, we know that the transition from phobicity to philicity occurs around $\varepsilon_{SL} \approx 5$ meV. Therefore, the sharp rise in $\Delta\Gamma$ observed at this point coincides with a change in the characteristic curvature of the liquid/vapor interface, namely from concavity to convexity in the direction of the vapor. This raises the third question to be addressed in this work: *why does the enhancement in Γ experience a sharp enhancement beyond $\varepsilon_{SL} \approx 5$ meV?*

To answer the questions posed thus far, we will first assess whether the presence of a TPCL alters the frequencies of the utilized modes within both the interfacial solid and liquid, followed by an examination of the orientation of the utilized vibrations. This will be achieved by analyzing the spectral mechanisms of interfacial energy transport within the meniscus system, and comparing them to those within the benchmark confined system at each wettability.

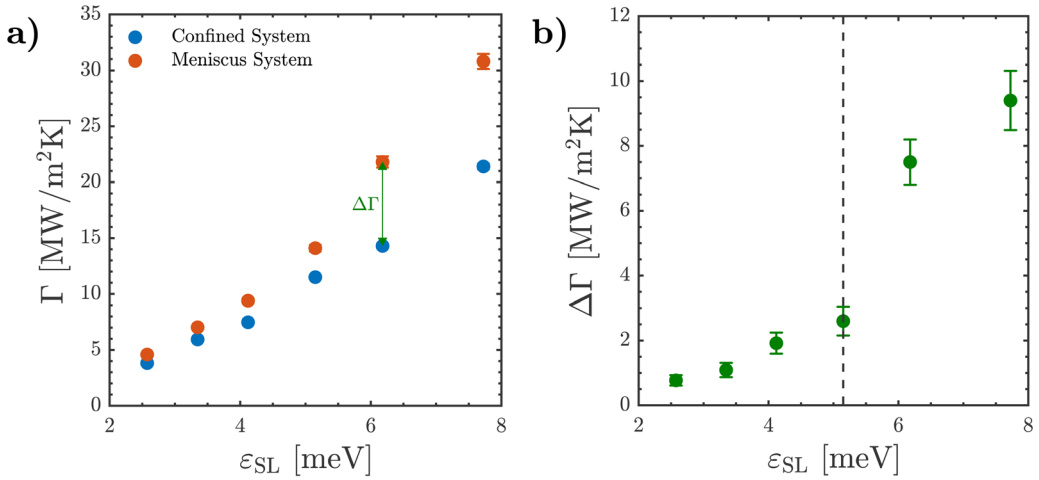

Fig. 4 (a) The solid/liquid interfacial thermal conductance accounting for the actual liquid contact area (Γ) for the confined (blue points) and meniscus (orange points) systems at various values of the solid/liquid interaction strength ε_{SL}. (b) The increase in Γ due to the presence of a meniscus ($\Delta\Gamma$) for different values of ε_{SL}.

Effect of meniscus on frequencies of utilized vibrations

In Fig. 5, the $q(\omega)_{L\to S}$ and $q(\omega)_{S\to L}$ distributions are presented for the confined and meniscus systems at three values of ε_{SL}. It can be observed that the magnitudes of the $q(\omega)_{L\to S}$ and $q(\omega)_{S\to L}$ distributions differ greatly across the two systems, because the meniscus and confined systems possess significantly different magnitudes of Γ for the same value of ε_{SL}. Attempting to compare two distributions of vastly different magnitudes would obscure any differences between them. Therefore, the $q(\omega)_{L\to S}$ and $q(\omega)_{S\to L}$ distributions of the two systems are normalized by setting the area beneath their curves to unity to facilitate their comparison in the remainder of this section. First, the normalized $q(\omega)_{L\to S}$ distributions of the meniscus and confined systems will be compared, followed by their normalized $q(\omega)_{S\to L}$ distributions.

Comparing the $q(\omega)_{L\to S}$ distributions. The normalized distributions of the spectral decompositions of heat flux within the interfacial solid ($q(\omega)_{L\to S}$) for both the confined (blue line) and meniscus (orange line) systems are shown in Fig. 6(i)–(iii). Three values of ε_{SL} from the cases presented in Fig. 4 are selected, with the dotted blue and orange lines representing the median value of that distribution. From Fig. 6(i)–(iii), it can be observed that there are no statistically significant differences in the distributions of $q(\omega)_{L\to S}$ between the meniscus and confined systems.

Comparing the $q(\omega)_{S\to L}$ distributions. Fig. 6(iv)–(vi) illustrate the normalized spectral decomposition of heat flux within the interfacial liquid ($q(\omega)_{S\to L}$) for both the confined and meniscus systems at the same magnitudes of ε_{SL}. From these plots, it is apparent that the normalized distributions of $q(\omega)_{S\to L}$ are virtually identical for both systems across all values of ε_{SL} as demonstrated by their near-perfect overlap, similar to the case of the interfacial solid. Once again, this means that the frequencies of the modes utilized within the interfacial liquid are similar across the two systems, regardless of ε_{SL}.

To rule out the presence of potential size effects, the normalized $q(\omega)_{L\to S}$ and $q(\omega)_{S\to L}$ distributions in the confined system at ε_{SL} = 2.5–5 meV are compared to those at a much larger nanochannel, as reported in our previous work.[40] As shown in Fig. S6 of the ESI,† the normalized $q(\omega)_{L\to S}$ and $q(\omega)_{S\to L}$ spectra are virtually identical across both nanochannels, implying the size of the nanochannel does not influence the spectral properties of interfacial energy transport.

Nonetheless, the enhancement in Γ due to the presence of a meniscus cannot be explained by a change in the frequencies of the vibrations utilized within the interfacial solid or liquid, and alternative mechanisms must be explored.

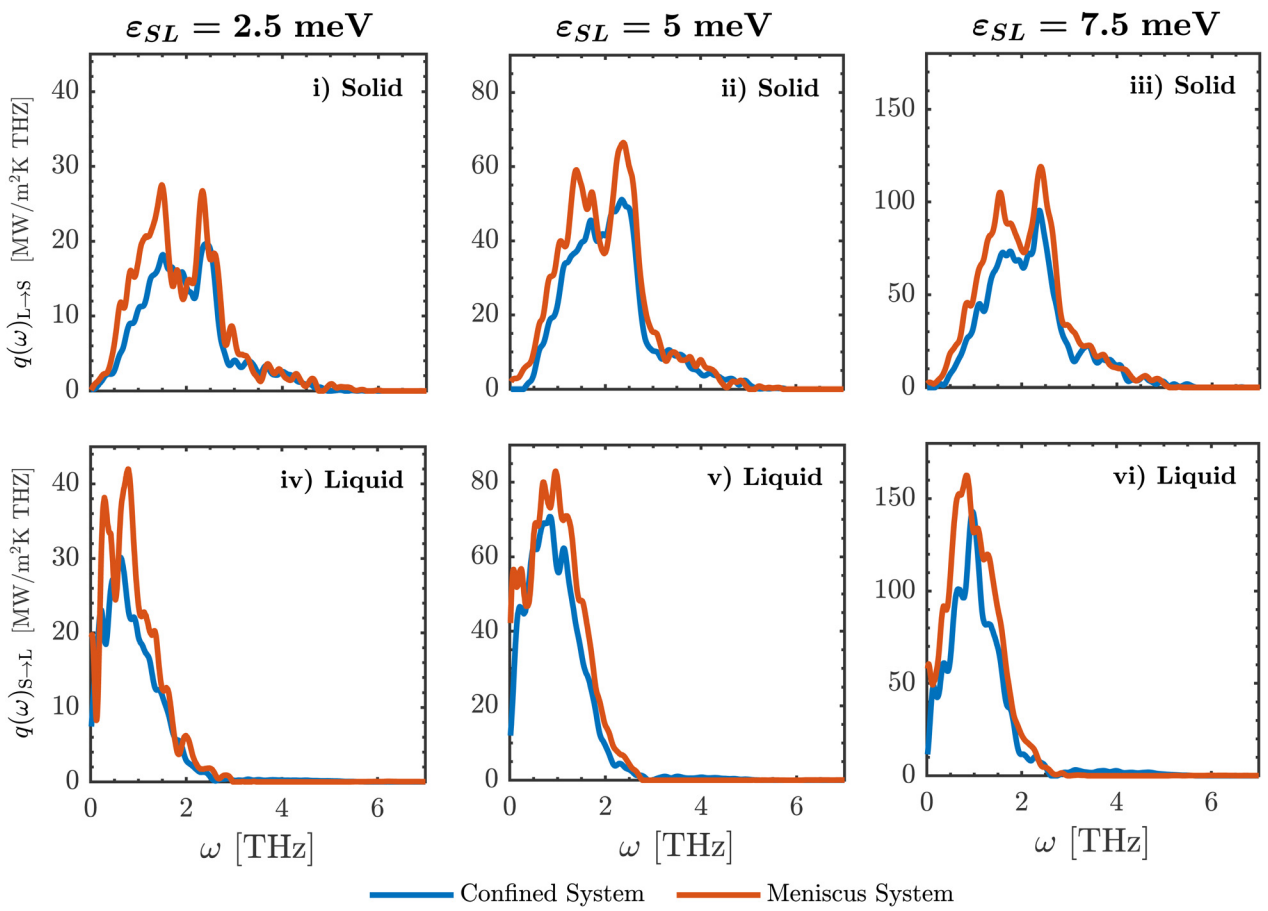

Fig. 5 Spectral decompositions of heat flux for the confined and meniscus systems at select values of the solid/liquid interaction strength ε_{SL} within the: (i)–(iii) interfacial solid ($q(\omega)_{L\to S}$) and (iv)–(vi) interfacial liquid ($q(\omega)_{S\to L}$).

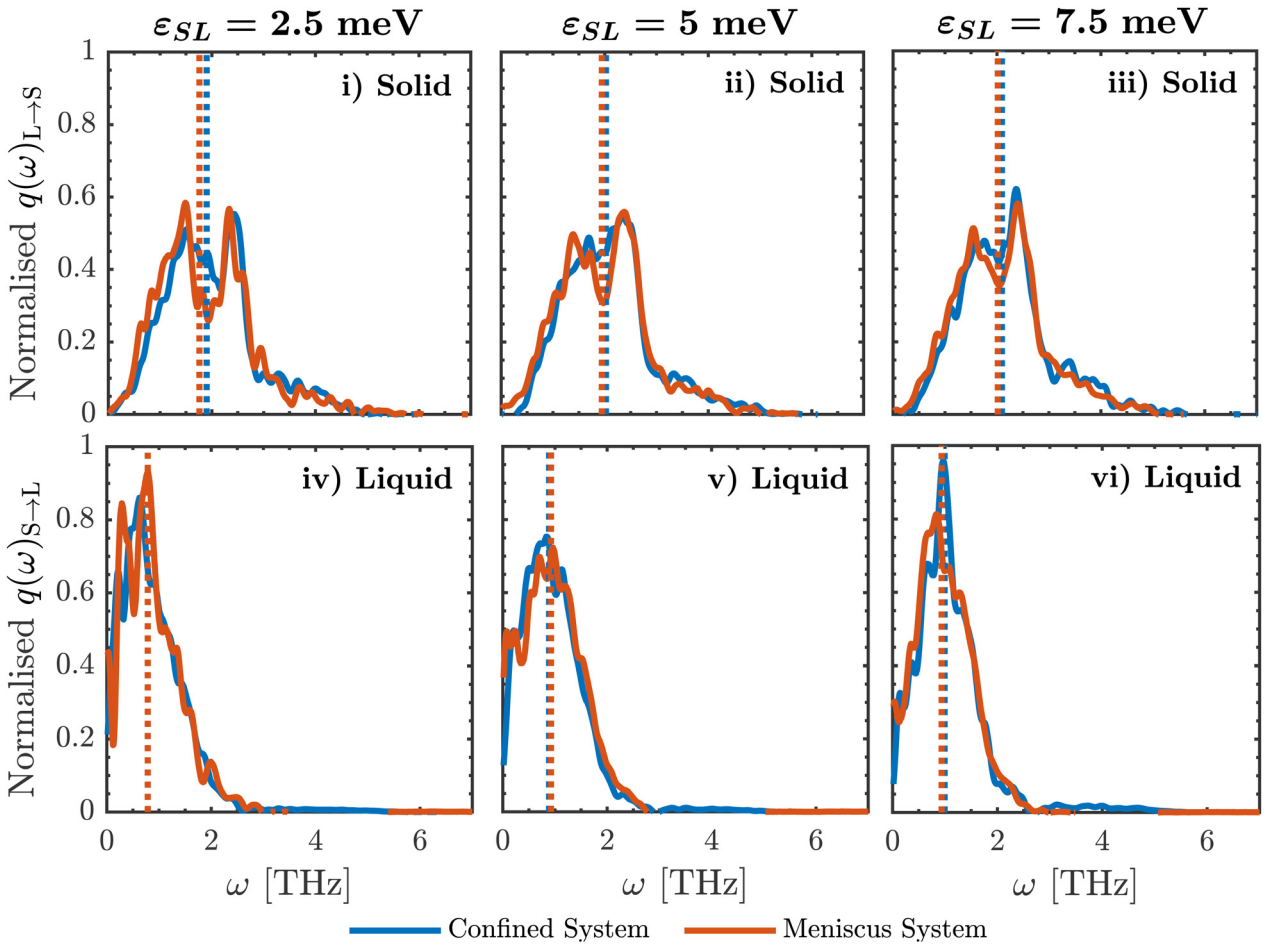

Fig. 6 Normalized spectral decompositions of heat flux for the confined and meniscus systems at select values of the solid/liquid interaction strength ε_{SL} within the (i)–(iii) interfacial solid ($q(\omega)_{L\to S}$) and (iv)–(vi) interfacial liquid ($q(\omega)_{S\to L}$).

Effect of meniscus on orientation of utilized vibrations

Rather than merely comparing the overall spectral distributions of $q(\omega)_{L\to S}$ and $q(\omega)_{S\to L}$, which probes whether the meniscus and confined systems utilize modes of different *frequencies*, these spectra can be further decomposed based on the *orientation* of the vibrations with respect to the plane of the interface.[44] As stated previously, differences in the orientation of utilized modes have been observed in the literature,[33,35,41] but this has not yet been studied at the TPCL. Thus, the next step is to analyze the contribution of the in-plane and out-of-plane modes towards the interfacial thermal conductance Γ.

The spectral distributions $q(\omega)_{L\to S}$ and $q(\omega)_{S\to L}$ can be decomposed into their out-of-plane ($q(\omega)^{\perp}_{L\to S}$, $q(\omega)^{\perp}_{S\to L}$) and in-plane ($q(\omega)^{\parallel}_{L\to S}$, $q(\omega)^{\parallel}_{S\to L}$) components using eqn (6) and (7), as presented in Fig. S3 and S4 of the ESI.† However, this merely quantifies the contributions of each *individual* vibrational frequency ω towards interfacial energy transport. An alternative metric is the *cumulative* contribution of the *entire range* of vibrational frequencies towards Γ. This can be obtained by computing the "spectral accumulation" of each distribution, calculated *via* their cumulative integration with respect to ω, as presented in eqn (8). Using this calculation, the separate contributions of in-plane and out-of-plane modes towards the total energy transported in each system can be compared across the meniscus and confined systems. Note that, as we are now interested in comparing the actual energetic contributions of each vibrational orientation rather than merely their spectral distribution, the spectral accumulations will not be normalized. First, this analysis will be conducted in the interfacial solid, followed by the interfacial liquid.

The representative examples of the cumulative spectral distribution for the confined liquid and the meniscus case are presented in Fig. 7(a) and 8(a). It should be noted that both cumulative spectral distributions under higher frequencies are approximately equal to the thermal conductance calculated by the use of eqn (1): $\Gamma = \Gamma(\omega \to \infty)_{L\to S} \approx \Gamma(\omega \to \infty)_{S\to L}$ (see Fig. S5 in the ESI†). The discrepancy between the two is caused by the statistical error in computing the spectral decomposition of heat flux within both media, in line with prior studies.[52]

Spectral accumulations within the interfacial solid. Fig. 7(a) shows the spectral accumulations of the $\Gamma(\omega)_{L\to S}$ distributions for both the meniscus and confined systems at the lowest value of ε_{SL} = 2.5 meV, accompanied by their further decomposition into their out-of-plane ($\Gamma(\omega)^{\perp}_{L\to S}$) and in-plane ($\Gamma(\omega)^{\parallel}_{L\to S}$) components. The panels thus present the following information:

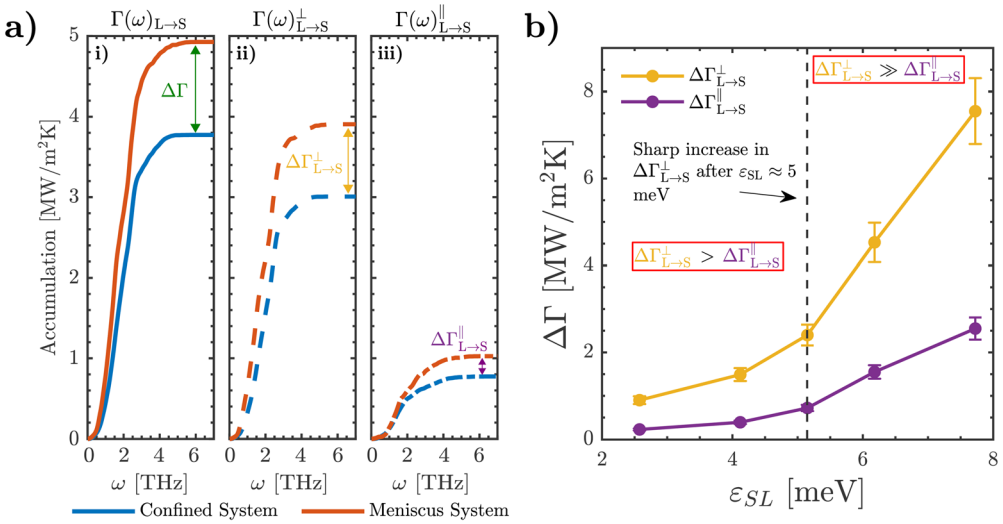

Fig. 7 (a) Accumulations of the non-normalized spectral decompositions of Γ within the interfacial solid for the: (i) total $\Gamma(\omega)_{L\to S}$ and its (ii) out-of-plane ($\Gamma(\omega)^{\perp}_{L\to S}$) and (iii) in-plane ($\Gamma(\omega)^{\parallel}_{L\to S}$) contributions for both the meniscus and confined systems at ε_{SL} = 2.5 meV. The spectral accumulations are obtained *via* cumulative integration of the original distribution. (b) The relationship between the components of $\Delta\Gamma$ within the interfacial solid ($\Delta\Gamma(\omega)^{\perp}_{L\to S}$, $\Delta\Gamma(\omega)^{\parallel}_{L\to S}$) for varying solid/liquid interaction strength ε_{SL}.

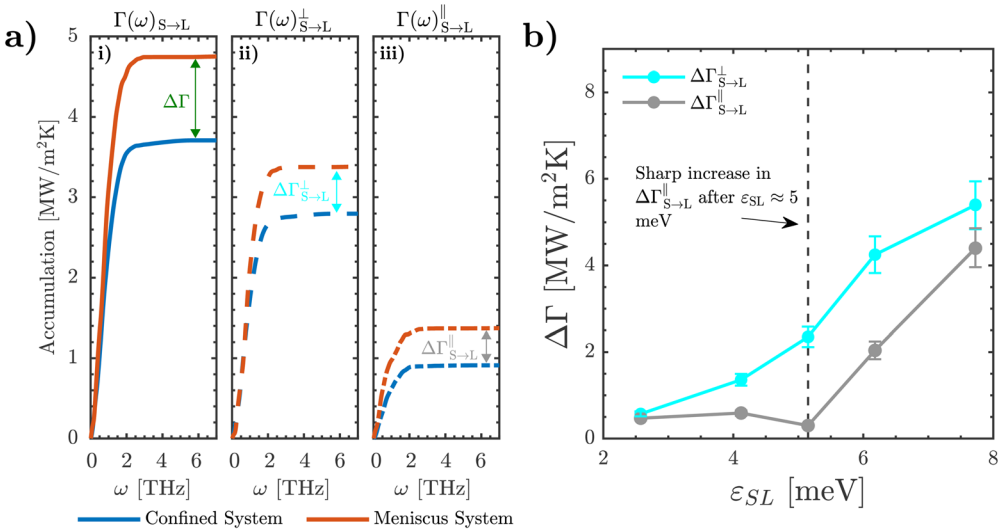

Fig. 8 (a) Accumulations of the non-normalized spectral decompositions of Γ within the interfacial liquid for the: (i) total $\Gamma(\omega)_{S\to L}$ and its (ii) out-of-plane ($\Gamma(\omega)^{\perp}_{S\to L}$) and (iii) in-plane ($\Gamma(\omega)^{\parallel}_{S\to L}$) contributions for both the meniscus and confined systems at ε_{SL} = 2.5 meV. (b) The relationship between the components of $\Delta\Gamma$ within the interfacial liquid ($\Delta\Gamma(\omega)^{\perp}_{S\to L}$, $\Delta\Gamma(\omega)^{\parallel}_{S\to L}$) for varying solid/liquid interaction strength ε_{SL}.

1. The leftmost panel (Fig. 7(a)(i)) illustrates the accumulations of the total $\Gamma(\omega)_{L\to S}$ distributions for both systems. The final value of each accumulation represents the actual magnitude of Γ of a given system, and the gap between the accumulations of the meniscus and confined systems represents the enhancement in Γ due to the meniscus $\Delta\Gamma$, which are identical to the values first shown in Fig. 4.

2. The middle panel (Fig. 7(a)(ii)) shows the accumulations of the out-of-plane component of energy transport within the interfacial solid $\Gamma(\omega)^{\perp}_{L\to S}$ for the two systems. Here, the gap between their accumulations represents the difference in the contributions of out-of-plane modes induced by the meniscus, denoted as $\Delta\Gamma^{\perp}_{IS}$ for the interfacial solid.

3. The rightmost panel (Fig. 7(a)(iii)) illustrates the accumulations of the in-plane component of heat transfer within the interfacial solid $\Gamma(\omega)^{\parallel}_{L\to S}$ for the meniscus and confined systems. Conversely, the gap between these accumulations represents the difference in the contributions of in-plane modes due to the presence of a meniscus, denoted as $\Delta\Gamma^{\parallel}_{IS}$ for the interfacial solid.

Analyzing Fig. 7(a)(i)–(iii), significant differences can be observed between the spectral accumulations of $\Gamma(\omega)^{\perp}_{L\to S}$ and $\Gamma(\omega)^{\parallel}_{L\to S}$ across the confined and meniscus systems at the lowest value of ε_{SL} = 2.5 meV. Specifically, the meniscus is seen to yield a large increase in $\Gamma(\omega)^{\perp}_{L\to S}$, but a relatively smaller increase in $\Gamma(\omega)^{\parallel}_{L\to S}$.

By quantifying the magnitude of the gaps between the accumulations of $\Gamma(\omega)^{\perp}_{\mathrm{L}\to\mathrm{S}}$ and $\Gamma(\omega)^{\parallel}_{\mathrm{L}\to\mathrm{S}}$ for the meniscus and confined systems, $\Delta\Gamma$ can be effectively decomposed within the interfacial solid into its out-of-plane ($\Delta\Gamma(\omega)^{\perp}_{\mathrm{L}\to\mathrm{S}}$) and in-plane ($\Delta\Gamma(\omega)^{\parallel}_{\mathrm{L}\to\mathrm{S}}$) components. Fig. 7(b) plots these decomposed values within the solid at each value of $\varepsilon_{\mathrm{SL}}$ studied, as derived from their spectral accumulations. From this plot, two observations can be made:

1. $\Delta\Gamma(\omega)^{\perp}_{\mathrm{L}\to\mathrm{S}}$ is significantly larger than $\Delta\Gamma(\omega)^{\parallel}_{\mathrm{L}\to\mathrm{S}}$ across all magnitudes of $\varepsilon_{\mathrm{SL}}$ considered. Thus, the enhancement in Γ due to the presence of a meniscus coincides with the increase in the utilization of out-of-plane modes in the interfacial solid across all values of $\varepsilon_{\mathrm{SL}}$ studied.

2. When $\varepsilon_{\mathrm{SL}} < 5$ meV, $\Delta\Gamma(\omega)^{\perp}_{\mathrm{L}\to\mathrm{S}}$ and $\Delta\Gamma(\omega)^{\parallel}_{\mathrm{L}\to\mathrm{S}}$ both increase monotonously. However, beyond $\varepsilon_{\mathrm{L}\to\mathrm{S}} > 5$ meV, both $\Delta\Gamma(\omega)^{\perp}_{\mathrm{L}\to\mathrm{S}}$ and $\Delta\Gamma(\omega)^{\parallel}_{\mathrm{L}\to\mathrm{S}}$ rise sharply. This sharp increase in the utilization of the in-plane and out-of-plane modes of the solid coincides with the sharp enhancement in $\Delta\Gamma$ that occurs around $\varepsilon_{\mathrm{SL}} \approx 5$ meV, initially seen in Fig. 4(b).

Note that these differences arise from the *transmitted* spectra (*i.e.* within the interfacial solid); next, we evaluate the influence of the meniscus on the modes utilized to *receive* energy by the liquid.

Spectral accumulations within the interfacial liquid. Fig. 8(a)(i)–(iii) similarly depict the accumulations of the $\Gamma(\omega)_{\mathrm{S}\to\mathrm{L}}$ distributions of the interfacial liquid for both the meniscus and confined systems at $\varepsilon_{\mathrm{SL}} = 2.5$ meV, alongside their out-of-plane ($\Gamma(\omega)^{\perp}_{\mathrm{S}\to\mathrm{L}}$) and in-plane ($\Gamma(\omega)^{\parallel}_{\mathrm{S}\to\mathrm{L}}$) components. As was the case with the interfacial solid, the presence of a meniscus gives rise to significant differences in the accumulations of $\Gamma(\omega)^{\perp}_{\mathrm{S}\to\mathrm{L}}$ and $\Gamma(\omega)^{\parallel}_{\mathrm{S}\to\mathrm{L}}$ between the confined and meniscus systems at the lowest value of $\varepsilon_{\mathrm{SL}}$; thus, this process is repeated across the entire range of values for $\varepsilon_{\mathrm{SL}}$.

Fig. 8(b) similarly depicts the decomposition of $\Delta\Gamma$ into its out-of-plane ($\Delta\Gamma(\omega)^{\perp}_{\mathrm{S}\to\mathrm{L}}$) and in-plane ($\Delta\Gamma(\omega)^{\parallel}_{\mathrm{S}\to\mathrm{L}}$) components within the liquid across the entire range of values for $\varepsilon_{\mathrm{SL}}$ studied. From this plot, four observations can be made:

1. When $\varepsilon_{\mathrm{SL}} = 2.5$ meV, $\Delta\Gamma(\omega)^{\perp}_{\mathrm{S}\to\mathrm{L}} \approx \Delta\Gamma(\omega)^{\parallel}_{\mathrm{S}\to\mathrm{L}}$. Thus, at this magnitude of $\varepsilon_{\mathrm{SL}}$, the enhancement in Γ can be equally divided into the rise in the utilization of both out-of-plane and in-plane modes in the interfacial liquid, contrary to the interfacial solid (where the out-of-plane component dominated).

2. As $\varepsilon_{\mathrm{SL}}$ is increased to 5 meV, $\Delta\Gamma(\omega)^{\perp}_{\mathrm{S}\to\mathrm{L}}$ rises monotonously, while $\Delta\Gamma(\omega)^{\parallel}_{\mathrm{S}\to\mathrm{L}}$ remains roughly unchanged (the origin of the small dip at 5 meV is not fully understood, but does not impact the remainder of this discussion). Consequently, when $\varepsilon_{\mathrm{SL}}$ is in the range 2.5–5 meV, $\Delta\Gamma(\omega)^{\perp}_{\mathrm{S}\to\mathrm{L}}$ is notably larger than $\Delta\Gamma(\omega)^{\parallel}_{\mathrm{S}\to\mathrm{L}}$, and the enhancement in Γ yielded by the meniscus coincides with an increase in the utilization of the out-of-plane modes of the liquid. This is in alignment with the interfacial solid in this range of values for $\varepsilon_{\mathrm{SL}}$.

3. Upon further increasing $\varepsilon_{\mathrm{SL}}$ beyond 5 meV, $\Delta\Gamma(\omega)^{\parallel}_{\mathrm{S}\to\mathrm{L}}$ rises sharply, while $\Delta\Gamma(\omega)^{\perp}_{\mathrm{S}\to\mathrm{L}}$ increases to a lesser degree. Consequently, the difference between the two shrinks. As a result, at the highest value of $\varepsilon_{\mathrm{SL}}$, the enhancement in Γ coincides with a rise in the utilization of both the in-plane and out-of-plane modes of the interfacial liquid, with the latter being more important.

4. The sharp increase in the utilization of the in-plane modes of the liquid $\Delta\Gamma(\omega)^{\parallel}_{\mathrm{S}\to\mathrm{L}}$ around $\varepsilon_{\mathrm{SL}} \approx 5$ meV coincides with the rise in $\Delta\Gamma$ that occurs around the same point, initially observed in Fig. 4(b).

From this set of spectral analyses, it is evident that the presence of a meniscus significantly impacts the orientation of the utilized modes within both the interfacial solid and liquid, which coincides with the observed enhancement in Γ. It is also evident that there are differences in spectral transmission between menisci for different $\varepsilon_{\mathrm{SL}}$. These are discussed in the next section.

Connecting spectral mechanisms to the presence and curvature of the meniscus

The large variation in $\varepsilon_{\mathrm{SL}}$ leads to the formation of menisci of vastly different curvatures, as shown in Fig. 9(b)–(d). To understand the relationship between the spectral mechanisms

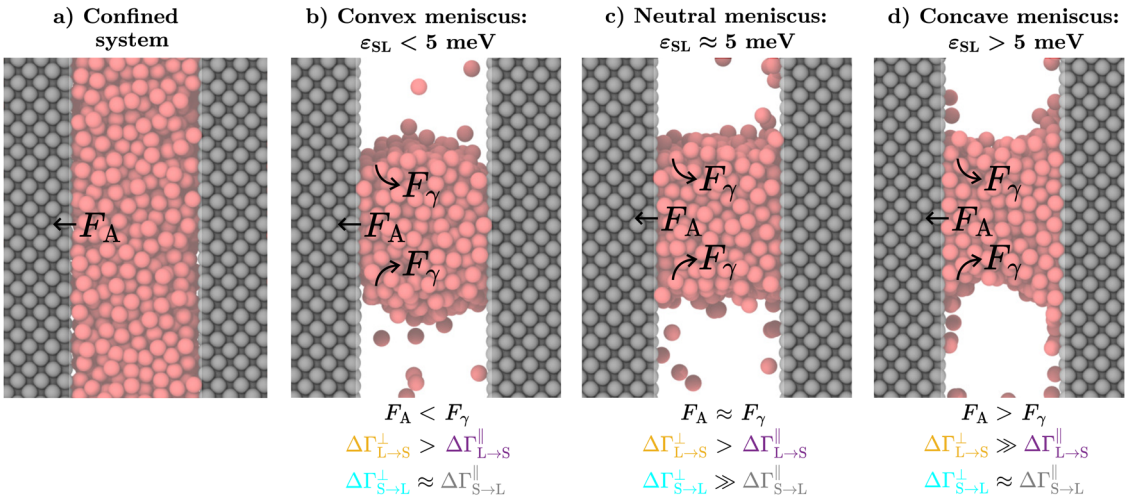

Fig. 9 A schematic showing the (a) confined system, demonstrating the adhesive force F_{A}; (b) convex meniscus for $\varepsilon_{\mathrm{SL}} < 5$ meV, with the adhesive force F_{A} and interfacial tension F_{γ} illustrated; (c) neutral meniscus for $\varepsilon_{\mathrm{SL}} \approx 5$ meV; and (d) concave meniscus for $\varepsilon_{\mathrm{SL}} > 5$ meV. The relative magnitude of F_{A} and F_{γ} in each case, as well as the dominant in-plane and out-of-plane mode increases within the solid and liquid, are included below (b)–(d).

described thus far and the curvature of the meniscus, the interfacial interactions between the three phases at the TPCL of each meniscus must first be examined. Following this, the role of the TPCL in inducing the spectral differences between the confined and meniscus systems will be described. Finally, the origins of the variation in these spectral differences induced by the change in the curvature of the TPCL will be discussed.

Interfacial Interactions at the TPCL. In the confined system (Fig. 9(a)), the liquid experiences an attractive force of adhesion towards the solid, resulting from the solid/liquid interfacial interactions. However, in the meniscus system the liquid/vapor interfacial liquid are pulled by interfacial tension towards the bulk of the meniscus. This liquid/vapor interfacial tension F_γ is independent of the magnitude of ε_{SL}, and for the liquid modeled in this work, $F_\gamma \approx 17.5$ mN m^{-1}.[53] Meanwhile, the length-averaged force of adhesion F_A is a function of ε_{SL}, and can be estimated from F_γ and the wetting angle θ.[54] This can be achieved *via*:

$$F_A = (1 + \cos\theta)F_\gamma. \quad (10)$$

Using eqn (10) and the wetting angles presented previously in Fig. 2, F_A can be estimated for each value of ε_{SL}, as shown in Fig. 10. Thus, the balance between F_A and F_γ with varying ε_{SL} gives rise to three distinct meniscus curvatures:

1. **Convex meniscus:** at the lowest value of ε_{SL}, it can be observed that the meniscus exhibits a pronounced convex shape, with a high curvature of the TPCLs it comprises, as illustrated in Fig. 9(b). This is caused by the magnitude of the interfacial tension F_γ exceeding the magnitude of the solid/liquid adhesive forces F_A (*i.e.* $F_A < F_\gamma$), as observed in Fig. 10. Due to these weak adhesion, the TPCL is not "pinned" to the surface and can move, leading to a high slip of the interfacial liquid.[55]

2. **Neutral meniscus:** as ε_{SL} is increased to 5 meV, the meniscus gradually reduces the curvature of its TPCLs, taking a neutral shape around $\varepsilon_{SL} \approx 5$ meV, as shown in Fig. 9(c). In this case, the magnitude of the interfacial tension F_γ is roughly equal to that of the adhesive forces F_A (*i.e.* $F_A \approx F_\gamma$), as seen in Fig. 10. As a result, the interfacial slip reduces, but is still non-negligible.[56]

3. **Concave meniscus:** as ε_{SL} is increased beyond 5 meV, the meniscus begins taking a concave shape, now increasing its curvature once again, as observed in Fig. 9(d). This is caused by the magnitude of F_A exceeding that of F_γ (*i.e.* $F_A > F_\gamma$), as shown in Fig. 10. Consequently, the TPCL becomes pinned, and the interfacial slip becomes negligible.[56]

Origins of spectral differences between confined and meniscus systems. In the solid, Fig. 7(b) showed that the increase in ε_{SL} to 5 meV, *i.e.* the transition from a convex meniscus (Fig. 9(b)) to a neutral meniscus (Fig. 9(c)), coincides with a rise in the utilization of the out-of-plane modes of the solid ($\Delta\Gamma(\omega)^{\perp}_{L\to S}$), accompanied by a smaller increase in the utilization of its in-plane modes ($\Delta\Gamma(\omega)^{\parallel}_{L\to S}$). Further increases in ε_{SL} beyond 5 meV, *i.e.* the transition from a neutral meniscus (Fig. 9(c)) to a concave one (Fig. 9(d)), coincide with sharp rises in the utilization of the out-of-plane ($\Delta\Gamma(\omega)^{\perp}_{L\to S}$) and in-plane ($\Delta\Gamma(\omega)^{\parallel}_{L\to S}$) modes of the solid.

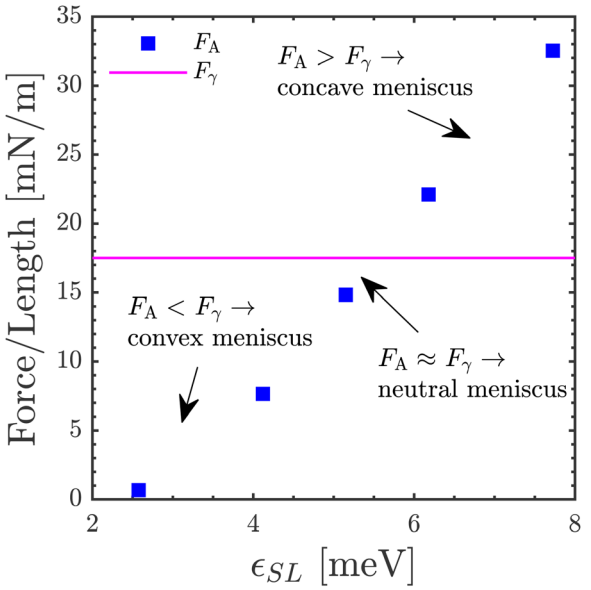

Fig. 10 The variation of the length-averaged force of adhesion F_A with the solid/liquid interaction strength ε_{SL} relative to the liquid/vapor interfacial tension F_γ.

In the liquid, Fig. 8(b) showed that the transition from a convex meniscus to a neutral one corresponds to a rise in the utilization of the out-of-plane modes of the liquid ($\Delta\Gamma(\omega)^{\perp}_{S\to L}$), and an insignificant change in the utilization of its in-plane modes ($\Delta\Gamma(\omega)^{\parallel}_{S\to L}$). Beyond $\varepsilon_{SL} \approx 5$ meV, the utilization of the out-of-plane modes in the liquid continues to increase monotonously, while the utilization of its in-plane modes increases sharply. These enhancements between the confined and meniscus systems, as well as the dependence of these enhancements on the wettability of the surface, can be explained in the following way:

1. **Solid:**

(a) Increase in out-of-plane utilization ($\Delta\Gamma(\omega)^{\perp}_{L\to S}$): it has been demonstrated that, at a solid/vapor interface, the out-of-plane modes within the solid are less hindered when compared to a solid/liquid interface, and are thus utilized to a larger degree.[45] This is consistent with our observations where the utilization of these out-of-plane modes is increased for the meniscus systems where a vapor region is present, when compared to the confined system which is fully liquid.

(b) Variation of out-of-plane utilization with meniscus shape: with increasing ε_{SL}, the reduction in the curvature of the meniscus exposes the solid at the TPCL to a larger number of vapor atoms, and a correspondingly smaller number of liquid atoms. Thus, the mechanism in (a) above is drastically magnified upon the transition from a neutral meniscus to a concave one, due to the significant reduction in the number of liquid atoms adjacent to the solid atoms at the TPCL. This likely induces the sharp rise in the utilization of the out-of-plane modes beyond $\varepsilon_{SL} \approx 5$ meV, previously observed in Fig. 7(b).

(c) Increase in in-plane utilization ($\Delta\Gamma(\omega)^{\parallel}_{L\to S}$): the interplay between the adhesive forces F_A and the interfacial tension F_γ localized on the solid atoms adjacent to the TPCL enables the solid to utilize its in-plane modes more effectively.

(d) Variation of in-plane utilization with meniscus shape: with increasing ε_{SL}, the resulting interfacial forces acting on the solid atoms of the TPCL increase steadily in magnitude,[57] yielding the steady increase in the utilization of the in-plane modes of the solid observed in Fig. 7(b) for $\varepsilon_{SL} < 5$ meV.

2. **Liquid:**

(a) Increase in out-of-plane ($\Delta\Gamma(\omega)^{\perp}_{L\rightarrow S}$) and in-plane ($\Delta\Gamma(\omega)^{\parallel}_{L\rightarrow S}$) utilization: similar to the solid, the interplay between the adhesive forces F_A and the interfacial tension F_γ localized on the liquid atoms in the TPCL acts as an additional dissipation mechanism for all received modes, facilitating their transmission from the solid into the liquid.

(b) Variation of out-of-plane utilization with meniscus shape: with increasing ε_{SL}, this mode dissipation is amplified, facilitating the transfer of the out-of-plane modes of the solid into out-of-plane modes within the liquid. This explains the rise in the utilization of the out-of-plane modes of the liquid observed in Fig. 8(b).

Transition from convex to neutral meniscus. Fig. 8(b) showed that the liquid experiences virtually no increase in the utilization of its in-plane modes ($\Delta\Gamma(\omega)^{\parallel}_{S\rightarrow L}$) when ε_{SL} is increased to 5 meV, *i.e.* upon the transition from a convex meniscus (Fig. 9(b)) to a neutral meniscus (Fig. 9(c)). This occurs because, despite the increase in the magnitude of F_A relative to F_γ, the interfacial slip that the liquid experiences is still significant,[55,56] and its in-plane modes cannot be effectively utilized.[44,45]

Transition from neutral to concave meniscus. With further increases in ε_{SL}, the curvature of the meniscus transition from a neutral meniscus (Fig. 9(c)) to a concave meniscus (Fig. 9(d)). Fig. 7(b) showed that this coincides with a sharp rise in the utilization of the in-plane modes of the solid ($\Delta\Gamma(\omega)^{\parallel}_{L\rightarrow S}$), while Fig. 8(b) similarly showed a sharp increase in the utilization of the in-plane modes of the liquid ($\Delta\Gamma(\omega)^{\parallel}_{S\rightarrow L}$). As discussed prior, the large increase the magnitude of the adhesion force F_A relative to the interfacial tension F_γ leads to the pinning of the TPCL, drastically reducing the slip of the interfacial liquid.[56] This significantly facilitates the utilization of the in-plane modes of the solid and liquid, consistent with prior observations where the transition from phobicity to philicity led to a rise in the utilization of in-plane modes.[33,35]

Conclusions

The impact of a meniscus on the solid/liquid interfacial thermal conductance (Γ) was studied at an LJ solid/liquid interface for various magnitudes of the solid/liquid interaction strength ε_{SL}. Across all values of ε_{SL}, the presence of a meniscus was found to yield a significant enhancement in Γ ($\Delta\Gamma$). This enhancement was found to rise monotonously until $\varepsilon_{SL} \approx 5$ meV, beyond which it increases sharply. To understand why the meniscus yields an enhancement in Γ, and why the magnitude of this enhancement rises sharply beyond $\varepsilon_{SL} \approx 5$ meV, the spectral decomposition of heat flux formalism was used to probe the interfacial solid and liquid, respectively.

The meniscus was shown to have negligible influence on the frequencies of the utilized vibrations in the interfacial solid or liquid. Instead, it was seen to influence the preferred orientation of the utilized vibrations. The monotonous enhancement in $\Delta\Gamma$ until $\varepsilon_{SL} \approx 5$ meV coincided with an increase in the utilization of the out-of-plane vibrations engaged in heat transfer within both the interfacial solid and liquid. This was found to be caused by the interplay between adhesive forces and interfacial tension at the TPCL, which facilitates the utilization of out-of-plane modes in both media.

The sharp enhancement in $\Delta\Gamma$ beyond $\varepsilon_{SL} \approx 5$ meV was found to be related to the sharp increases in the utilization of the in-plane vibrations within both the interfacial solid and liquid, accompanied by a sharp rise in the utilization of the out-of-plane modes of the solid. This was found to be related to the drastic reduction in the slip of the interfacial liquid upon the transition from a neutral meniscus to a concave one. These results elucidate heat transfer processes at the TPCL, which are particularly relevant to state-of-the-art two-phase evaporators for integrated circuit cooling, among other applications.

Data availability

The code for LAMMPS used to run the simulations in this study can be found at **https://www.lammps.org** with DOI **https://doi.org/10.1016/j.cpc.2021.108171**. The version of the code employed for this study is version lammps-15Jun2023.

Conflicts of interest

There are no conflicts to declare.

Acknowledgements

This research is supported by ANR project ''PROMENADE'' no. ANR-23-CE50-0008. Molecular simulations were conducted using HPC resources from GENCI-TGCC and GENCI-IDRIS (no. A0150913052), as well as resources provided by the EXPLOR Center hosted by the University of Lorraine. S. P. thanks the Leverhulme Trust for the support provided through the Early Career Fellowship ECF-2021-137. R. P. is supported by the UKRI Frontier Guarantee Grant EP/Y036107/1.

References

1 P. A. Raghupathi and S. G. Kandlikar, Contact line region heat transfer mechanisms for an evaporating interface, *Int. J. Heat Mass Transfer*, 2016, **95**, 296–306.
2 P. A. Raghupathi and S. G. Kandlikar, Pool boiling enhancement through contact line augmentation, *Appl. Phys. Lett.*, 2017, **110**, 2014101.
3 K. Sefiane and A. Kosar, Prospects of heat transfer approaches to dissipate high heat fluxes: opportunities and challenges, *Appl. Therm. Eng.*, 2022, **215**, 118990.
4 D. F. Hanks, Z. Lu, J. Sircar, T. R. Salamon, D. S. Antao, K. R. Bagnall, B. Barabadi and E. N. Wang, Nanoporous

membrane device for ultra high heat flux thermal management, *Microsyst. Nanoeng.*, 2018, **4**, 1–10.

5 D. F. Hanks, Z. Lu, J. Sircar, I. Kinefuchi, K. R. Bagnall, T. R. Salamon, D. S. Antao, B. Barabadi and E. N. Wang, High heat flux evaporation of low surface tension liquids from nanoporous membranes, *ACS Appl. Mater. Interfaces*, 2020, **12**, 7232–7238.

6 A. Assy, S. Lefèvre, P. O. Chapuis and S. Gomès, Analysis of heat transfer in the water meniscus at the tip-sample contact in scanning thermal microscopy, *J. Phys. D: Appl. Phys.*, 2014, **47**, 20–25.

7 J. Bodzenta, A. Kamierczak-Bałata and K. Harris, Quantitative thermal measurement by the use of scanning thermal microscope and resistive thermal probes, *J. Appl. Phys.*, 2020, **127**, 031103.

8 Y. Zhang, W. Zhu, F. Hui, M. Lanza, T. Borca-Tasciuc and M. Muñoz Rojo, A Review on Principles and Applications of Scanning Thermal Microscopy (SThM), *Adv. Funct. Mater.*, 2020, **30**, 1900892.

9 J. Qiu, D. Huo and Y. Xia, Phase-Change Materials for Controlled Release and Related Applications, *Adv. Mater.*, 2020, **32**, 1–21.

10 R. Jilte, A. Afzal and S. Panchal, A novel battery thermal management system using nano-enhanced phase change materials, *Energy*, 2021, **219**, 119564.

11 X. Yan, J. Xu, Z. Meng, J. Xie and H. Wang, A New Mechanism of Light-Induced Bubble Growth to Propel Microbubble Piston Engine, *Small*, 2020, **16**, 1–15.

12 M. Rivetti, T. Salez, M. Benzaquen, E. Raphaël and O. Bäumchen, Universal contact-line dynamics at the nanoscale, *Soft Matter*, 2015, **11**, 9247–9253.

13 P. C. Stephan and C. A. Busse, Analysis of the heat transfer coefficient of grooved heat pipe evaporator walls, *Int. J. Heat Mass Transfer*, 1992, **35**, 383–391.

14 K. Ibrahem, M. F. Abd Rabbo, T. Gambaryan-Roisman and P. Stephan, Experimental investigation of evaporative heat transfer characteristics at the 3-phase contact line, *Exp. Therm. Fluid Sci.*, 2010, **34**, 1036–1041.

15 C. Kunkelmann, K. Ibrahem, N. Schweizer, S. Herbert, P. Stephan and T. Gambaryan-Roisman, The effect of three-phase contact line speed on local evaporative heat transfer: experimental and numerical investigations, *Int. J. Heat Mass Transfer*, 2012, **55**, 1896–1904.

16 S. C. Maroo and J. N. Chung, Fundamental roles of nonevaporating film and ultrahigh heat flux associated with nanoscale meniscus evaporation in nucleate boiling, *J. Heat Transfer*, 2013, **135**, 1–10.

17 J. J. Zhao, M. Huang, Q. Min, D. M. Christopher and Y. Y. Duan, Near-wall liquid layering, velocity slip, and solid–liquid interfacial thermal resistance for thin-film evaporation in microchannels, *Nanoscale Microscale Thermophys. Eng.*, 2011, **15**, 105–122.

18 H. Han, C. Schlawitschek, N. Katyal, P. Stephan, T. Gambaryan-Roisman, F. Leroy and F. Müller-Plathe, Solid–Liquid Interface Thermal Resistance Affects the Evaporation Rate of Droplets from a Surface: A Study of Perfluorohexane on Chromium Using Molecular Dynamics and Continuum Theory, *Langmuir*, 2017, **33**, 5336–5343.

19 B. Ma, K. Guye, B. Dogruoz and D. Agonafer, Molecular dynamics simulations of thin-film evaporation: the influence of interfacial thermal resistance on a graphene-coated heated silicon substrate, *Appl. Therm. Eng.*, 2021, **195**, 117142.

20 L. Klochko, V. Mandrolko, G. Castanet, G. Pernot, F. Lemoine, K. Termentzidis, D. Lacroix and M. Isaiev, Molecular dynamics simulation of thermal transport across a solid/liquid interface created by a meniscus, *Phys. Chem. Chem. Phys.*, 2023, **25**, 3298–3308.

21 N. Shenogina, R. Godawat, P. Keblinski and S. Garde, How wetting and adhesion affect thermal conductance of a range of hydrophobic to hydrophilic aqueous interfaces, *Phys. Rev. Lett.*, 2009, **102**, 1–4.

22 S. Ge and M. Chen, Vibrational coupling and Kapitza resistance at a solid–liquid interface, *Int. J. Thermophys.*, 2013, **34**, 64–77.

23 J. A. Tomko, D. H. Olson, A. Giri, J. T. Gaskins, B. F. Donovan, S. M. O'Malley and P. E. Hopkins, Nanoscale Wetting and Energy Transmission at Solid/Liquid Interfaces, *Langmuir*, 2019, **35**, 2106–2114.

24 C. U. Gonzalez-Valle and B. Ramos-Alvarado, Molecular Dynamics Simulations of Wettability, Thermal Transport, and Interfacial Liquid Structuring at the Nanoscale in Polar Solid–Liquid Interfaces, *ACS Appl. Nano Mater.*, 2021, **4**, 3821–3832.

25 D. Alexeev, J. Chen, J. H. Walther, K. P. Giapis, P. Angelikopoulos and P. Koumoutsakos, Kapitza Resistance between Few-Layer Graphene and Water: Liquid Layering Effects, *Nano Lett.*, 2015, **15**, 5744–5749.

26 Y. Ma, Z. Zhang, J. Chen, K. Sääskilahti, S. Volz and J. Chen, Ordered water layers by interfacial charge decoration leading to an ultra-low Kapitza resistance between graphene and water, *Carbon*, 2018, **135**, 263–269.

27 X. Peng, P. Jiang, Y. Ouyang, S. Lu, W. Ren and J. Chen, Reducing Kapitza resistance between graphene/water interface via interfacial superlattice structure, *Nanotechnology*, 2022, **33**, 035707.

28 S. Li, Y. Chen, J. Zhao, C. Wang and N. Wei, Atomic structure causing an obvious difference in thermal conductance at the Pd–H_2O interface: a molecular dynamics simulation, *Nanoscale*, 2020, **12**, 17870–17879.

29 S. Alosious, S. K. Kannam, S. P. Sathian and B. D. Todd, Effects of Electrostatic Interactions on Kapitza Resistance in Hexagonal Boron Nitride-Water Interfaces, *Langmuir*, 2022, **38**, 8783–8793.

30 H. Han, S. Mérabia and F. Müller-Plathe, Thermal Transport at Solid–Liquid Interfaces: High Pressure Facilitates Heat Flow through Nonlocal Liquid Structuring, *J. Phys. Chem. Lett.*, 2017, **8**, 1946–1951.

31 S. Li, Y. Chen, Z. Li, J. Zhao and N. Wei, Role of hydrogen bonds in thermal conductance at the graphene oxide-H_2O interface, *Int. J. Heat Mass Transfer*, 2022, **183**, 122125.

32 B. Ramos-Alvarado, S. Kumar and G. P. Peterson, Solid–Liquid Thermal Transport and Its Relationship with

Wettability and the Interfacial Liquid Structure, *J. Phys. Chem. Lett.*, 2016, **7**, 3497–3501.
33 B. Ramos-Alvarado and S. Kumar, Spectral Analysis of the Heat Flow Across Crystalline and Amorphous Si–Water Interfaces, *J. Phys. Chem. C*, 2017, **121**, 11380–11389.
34 C. U. Gonzalez-Valle, S. Kumar and B. Ramos-Alvarado, Thermal Transport across SiC-Water Interfaces, *ACS Appl. Mater. Interfaces*, 2018, **10**, 29179–29186.
35 C. U. Gonzalez-Valle and B. Ramos-Alvarado, Spectral mapping of thermal transport across SiC–water interfaces, *Int. J. Heat Mass Transfer*, 2019, **131**, 645–653.
36 A. Anandakrishnan, B. Ramos-Alvarado, S. K. Kannam and S. P. Sathian, Effects of interfacial molecular mobility on thermal boundary conductance at solid–liquid interface, *J. Chem. Phys.*, 2023, **158**, 094710.
37 J. Chen, X. Xu, J. Zhou and B. Li, Interfacial thermal resistance: past, present, and future, *Rev. Mod. Phys.*, 2022, **94**, 25002.
38 C. Qian, Y. Wang, H. He, F. Huo, N. Wei and S. Zhang, Lower Limit of Interfacial Thermal Resistance across the Interface between an Imidazolium Ionic Liquid and Solid Surface, *J. Phys. Chem. C*, 2018, **122**, 22194–22200.
39 C. Qian, B. Ding, Z. Wu, W. Ding, F. Huo, H. He, N. Wei, Y. Wang and X. Zhang, Ultralow Thermal Resistance across the Solid–Ionic Liquid Interface Caused by the Charge-Induced Ordered Ionic Layer, *Ind. Eng. Chem. Res.*, 2019, **58**, 20109–20115.
40 A. El-Rifai, S. Perumanath, M. K. Borg and R. Pillai, Unraveling the Regimes of Interfacial Thermal Conductance at a Solid/Liquid Interface, *J. Phys. Chem. C*, 2024, **128**, 8408–8417.
41 T. Zhou, H. K. Chilukoti, Z. Wu and F. Müller-Plathe, Effect of Defects on the Interfacial Thermal Conductance betweenn-Heneicosane in Solid and Liquid Phases and a Graphene Monolayer, *J. Phys. Chem. C*, 2021, **125**, 14149–14162.
42 A. P. Thompson, H. M. Aktulga, R. Berger, D. S. Bolintineanu, W. M. Brown, P. S. Crozier, P. J. in 't Veld, A. Kohlmeyer, S. G. Moore and T. D. Nguyen, *et al.*, LAMMPS – a flexible simulation tool for particle-based materials modeling at the atomic, meso, and continuum scales, *Comput. Phys. Commun.*, 2022, **271**, 108171.
43 M. P. Allen and D. J. Tildesley, *Computer simulation of liquids*, Oxford University Press, 2017.
44 K. Sääskilahti, J. Oksanen, J. Tulkki and S. Volz, Spectral mapping of heat transfer mechanisms at liquid–solid interfaces, *Phys. Rev. E*, 2016, **93**, 1–8.
45 A. Giri, J. L. Braun and P. E. Hopkins, Implications of interfacial bond strength on the spectral contributions to thermal boundary conductance across solid, liquid, and gas interfaces: a molecular dynamics study, *J. Phys. Chem. C*, 2016, **120**, 24847–24856.
46 M. Isaiev, S. Burian, L. Bulavin, M. Gradeck, F. Lemoine and K. Termentzidis, Efficient tuning of potential parameters for liquid–solid interactions, *Mol. Simul.*, 2016, **42**, 910–915.
47 P. B. Miranda, L. Xu, Y. R. Shen and M. Salmeron, Icelike water monolayer adsorbed on mica at room temperature, *Phys. Rev. Lett.*, 1998, **81**, 5876–5879.
48 P. Geysermans, D. Gorse and V. Pontikis, Molecular dynamics study of the solid–liquid interface, *J. Chem. Phys.*, 2000, **113**, 6382–6389.
49 M. F. Reedijk, J. Arsic, F. F. Hollander, S. A. de Vries and E. Vlieg, Liquid Order at the Interface of KDP Crystals with Water: evidence for Icelike Layers, *Phys. Rev. Lett.*, 2003, **90**, 4.
50 Y. Kauffmann, S. H. Oh, C. T. Koch, A. Hashibon, C. Scheu, M. Rühle and W. D. Kaplan, Quantitative analysis of layering and in-plane structural ordering at an alumina–aluminum solid–liquid interface, *Acta Mater.*, 2011, **59**, 4378–4386.
51 S. A. Deshmukh and S. K. Sankaranarayanan, Atomic scale characterization of interfacial water near an oxide surface using molecular dynamics simulations, *Phys. Chem. Chem. Phys.*, 2012, **14**, 15593–15605.
52 C. U. Gonzalez-Valle, L. E. Paniagua-Guerra and B. Ramos-Alvarado, Implications of the Interface Modeling Approach on the Heat Transfer across Graphite-Water Interfaces, *J. Phys. Chem. C*, 2019, **123**, 22311–22323.
53 D. Zhou, M. Zeng, J. Mi and C. Zhong, Theoretical study of phase transition, surface tension, and nucleation rate predictions for argon, *J. Phys. Chem. B*, 2011, **115**, 57–63.
54 J. Israelachvili, *Intermolecular and Surface Forces*, 2011.
55 X. Geng, M. Yu, W. Zhang, Q. Liu, X. Yu and Y. Lu, Slip length and structure of liquid water flowing past atomistic smooth charged walls, *Sci. Rep.*, 2019, **9**, 18957.
56 V. Mandrolko, G. Castanet, S. Burian, Y. Grosu, L. Klochko, D. Lacroix and M. Isaiev, Features of the contact angle hysteresis at the nanoscale: a molecular dynamics insight, *Phys. Fluids*, 2024, **36**, 052012.
57 J. Fan, J. De Coninck, H. Wu and F. Wang, Microscopic Origin of Capillary Force Balance at Contact Line, *Phys. Rev. Lett.*, 2020, **124**, 125502.